



Article

Global Dynamics and Bifurcations of an Oscillator with Symmetric Irrational Nonlinearities

Rong Liu and Huilin Shang *

School of Mechanical Engineering, Shanghai Institute of Technology, Shanghai 201418, China

* Correspondence: shanghuilin@sit.edu.cn

Abstract: This study's objective is an irrationally nonlinear oscillating system, whose bifurcations and consequent multi-stability under the circumstances of single potential well and double potential wells are investigated in detail to further reveal the mechanism of the transition of resonance and its utilization. First, static bifurcations of its nondimensional system are discussed. It is found that variations of two structural parameters can induce different numbers and natures of potential wells. Next, the cases of mono-potential wells and double wells are explored. The forms and stabilities of the resonant responses within each potential well and the inter-well resonant responses are discussed via different theoretical methods. The results show that the natural frequencies and trends of frequency responses in the cases of mono- and double-potential wells are totally different; as a result of the saddle-node bifurcations of resonant solutions, raising the excitation level or frequency can lead to the coexistence of bistable responses within each well and cause an inter-well periodic response. Moreover, in addition to verifying the accuracy of the theoretical prediction, numerical results considering the disturbance of initial conditions are presented to detect complicated dynamical behaviors such as jump between coexisting resonant responses, intra-well period-two responses and chaos. The results herein provide a theoretical foundation for designing and utilizing the multi-stable behaviors of irrationally nonlinear oscillators.

Keywords: irrational nonlinearity; multi-stable dynamics; hidden attractor; fractal; chaos



Citation: Liu, R.; Shang, H. Global Dynamics and Bifurcations of an Oscillator with Symmetric Irrational Nonlinearities. *Fractal Fract.* **2023**, *7*, 888. <https://doi.org/10.3390/fractalfract7120888>

Academic Editor: Haci Mehmet Baskonus

Received: 11 November 2023

Revised: 11 December 2023

Accepted: 14 December 2023

Published: 18 December 2023



Copyright: © 2023 by the authors. Licensee MDPI, Basel, Switzerland. This article is an open access article distributed under the terms and conditions of the Creative Commons Attribution (CC BY) license (<https://creativecommons.org/licenses/by/4.0/>).

1. Introduction

Mechanical oscillators with irrational nonlinearities have attracted much attention as they are especially suitable for kinematic energy harvesting [1,2] and the vibration isolation of precision instruments and low-fragility equipment [3,4]. These structures are simply and easily implemented as they are composed of concentrated masses and inclined springs with linear stiffness [5]. Even though the restoring resistances provided by the springs are linear, their resulting actions on the mass can be irrationally nonlinear due to the geometrical configurations [6]. In the presence of damping and external excitation, these oscillatory systems can exhibit rich dynamical behaviors [7].

Due to their potential values in various applications, the design of these structures and the investigation of their dynamics has received growing interest in recent years. By utilizing the allocation of two horizontal and four inclined linear springs, Han and Cao [8] designed a nonlinear oscillator that exhibited intricate equilibrium bifurcations and chaotic behaviors under the perturbations of viscous damping and the ambient excitation. A mechanical network with irrational nonlinearities was proposed in which each unit consisted of a lumped mass and two symmetric inclined springs [9,10]. Under the excitation of the network being loaded at one of its ends via the modulated signal, the conditions for modulational instability were found to be sensitive to the springs' angle of inclination as well as the dissipative coefficient. A class of rotating pendulum systems with irrational nonlinearity were proposed, and its various kinds of bifurcations and limit cycles were then analytically validated by the numerical results [11,12]. As a result, smooth or discontinuous

dynamics, such as coexisting periodic motions and the transition of complex motion depending upon the value of a structural parameter, was demonstrated [12]. On this basis, Liu et al. [13] explored a new bursting oscillation of this oscillator, employed three cases of excitation patterns for the investigation of the complex bursting behaviors and analyzed the principle behind the slow-bursting responses and the equilibrium stability via the method of multiple scales (MMS). Novel suspension vibration reduction systems with geometric nonlinear damping were put forward by the configuration of four springs with linear stiffness, and their performance for vibration isolation under impact and random excitations was then analyzed via numerical calculations [14]. Li and Cao [15] proposed a smooth and discontinuous oscillatory system with an irrational nonlinearity, obtained the primary resonant solutions through applying the extended averaging method and then illustrated the complicated dynamical behaviors both numerically and experimentally [16]. Based on these findings, Wang et al. [17] studied the global dynamical behaviors and bifurcations for that oscillator with dry friction. The transition of its dynamics from the continuous system with irrational nonlinearity to the piecewise linear system was illustrated via numerical simulations and bifurcation diagrams. Han et al. [18] studied the stochastic response of the smooth and discontinuous oscillator under harmonic excitation and Gaussian white noise by using direct Monte Carlo simulations. Another irrationally nonlinear oscillator configured by two inclined springs and a lumped mass was proposed in Ref. [19], and its equilibrium bifurcations, periodic solutions and homoclinic bifurcation were discussed analytically [20]. For the design of oscillating-body wave energy converters, Zhang and Yang [21] proposed a nonlinear power take-off system that used a pair of oblique springs and a linear damper. The influences of the structural parameters on its power capture performance were evaluated by numerically calculating the motion response of the wave energy converting system. Qin et al. [22] considered a typical linkage-slider oscillator and intensively discussed the initial-sensitive phenomena emanating from the system such as snap through, locking instability and chaotic response.

According to the above-mentioned literature, complex dynamical behaviors such as multi-stability [23,24] and chaotic oscillation [25,26] commonly occur in oscillatory systems with strong irrational nonlinearities. Among these dynamical behaviors, higher-amplitude or large-extent inter-well responses are more desirable due to their engineering applications in kinematic energy harvesting and vibrating isolation [27]. In this case, the variation of initial conditions may induce the change in the final dynamical behavior. Accordingly, it is necessary for researchers to extend the investigation of the effects of initial conditions on achieving the largest-amplitude final response. Castro et al. [28] carried out a specific analysis of a structural system composed by a pair of coupled bistable von Mises trusses and found that the fractal basins of attraction of the attractors could trigger the loss of dynamic integrity and thus the reliability of the structure. Regarding the SD oscillator under harmonic excitation, Wang and Shang [29] investigated jump among periodic attractors, period-three responses and chaos caused by variations in the excitation level and initial states. Nevertheless, there are still very few reports concerning the effects of structural parameters in combination with initial conditions on inducing large-amplitude final dynamics of these oscillators. As a result, there is a large gap between the utilization and comprehension of the multi-stability characteristics of the irrationally nonlinear oscillators.

Based on the above statements, we regard a typical irrationally nonlinear oscillatory system as the main objective and clarify the effects of its structural parameters, ambient excitation and initial conditions on the overall multi-stable dynamics. The subsequent sections are arranged as follows: Section 2 introduces the geometrically nonlinear structure, its oscillatory system, the corresponding nondimensional system and the distances that induce static multi-stability. Following this, Section 3 analytically discusses resonant responses in the cases of mono-potential wells and double-potential wells. Section 4 then exhibits the dynamic responses and multi-stable transitions from the viewpoint of the

basins of attraction in order to validate the accuracy of the analysis. Some important conclusions are presented in Section 5.

2. Static Analysis of the Irrationally Nonlinear Oscillator

In this section, we focus on a class of nonlinear oscillators consisting of a collar of negligible size and two obliquely set up springs that connect to it by smooth pins [19], as depicted in Figure 1. Here, m denotes the mass of the collar; X , \dot{X} and \ddot{X} are the displacement, velocity and acceleration of the collar at the time t , respectively. The parameters k and L represent the stiffness coefficient and the free length of the elastic springs, respectively. The parameter h represents the vertical distance between each support and the simply supported beam which is supposed to be a rigid body; a is the initial horizontal distance between the collar and each fixed pin, namely, the half distance between two fixed pins; and P is the excitation loaded on the collar with the amplitude F and the frequency Ω . When considering the collar under a damping force proportional to the velocity of the collar in the horizontal direction with the damping coefficient δ , its governing equation can be constructed by applying Newton's second law as follows:

$$m\ddot{X} + \delta\dot{X} + k(X+a)\left(1 - \frac{L}{\sqrt{(X+a)^2 + h^2}}\right) + k(X-a)\left(1 - \frac{L}{\sqrt{(X-a)^2 + h^2}}\right) = F \cos \Omega t. \quad (1)$$

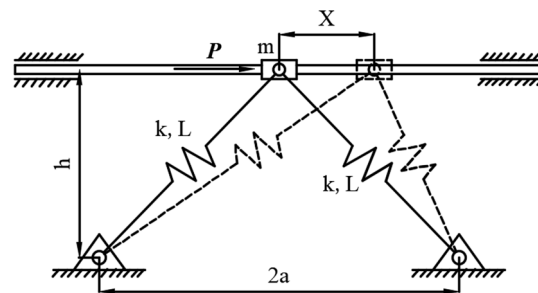


Figure 1. Oscillator composed of a collar and two inclined elastic springs.

As can be seen in Equation (1), the resultant of the restoring forces of the two springs in the horizontal direction has two irrationally and fractionally nonlinear terms, which illustrates a strongly irrational nonlinearity of the oscillating system as a result of the configuration of the elastic springs.

Introducing the following dimensionless variables

$$x = \frac{X}{L}, \omega_0^2 = \frac{k}{m}, \alpha = \frac{a}{L}, \beta = \frac{h}{L}, \zeta = \frac{\delta}{2m\omega_0}, f = \frac{F}{kL}, \omega = \frac{\Omega}{\omega_0}, T = \omega_0 t \quad (2)$$

into Equation (1), it becomes a non-dimensional dynamical system, i.e.,

$$\ddot{x} + 2\zeta\dot{x} + (x+\alpha)\left(1 - \frac{1}{\sqrt{(x+\alpha)^2 + \beta^2}}\right) + (x-\alpha)\left(1 - \frac{1}{\sqrt{(x-\alpha)^2 + \beta^2}}\right) = f \cos \omega T. \quad (3)$$

It is a smooth system for $\beta > 0$. Conversely, it is a discontinuous one at $\beta = 0$, namely,

$$\dot{x} = y, \dot{y} = -2\zeta y - 2x - \text{sign}(x+\alpha) - \text{sign}(x-\alpha) + f \cos \omega T. \quad (4)$$

In this case, there is no distance between the horizontal beam and each fixed pin in Figure 1, which is impractical for making use of the geometric configuration and its nonlinear characteristics in the applications of the structure. Hence, in this research, it is

assumed that $\beta > 0$; hence, the oscillatory system we study is smooth. Its unperturbed system can be written as

$$\dot{x} = y, \dot{y} = -(x + \alpha)\left(1 - \frac{1}{\sqrt{(x + \alpha)^2 + \beta^2}}\right) - (x - \alpha)\left(1 - \frac{1}{\sqrt{(x - \alpha)^2 + \beta^2}}\right). \quad (5)$$

The potential function and Hamiltonian function are

$$V(x) = x^2 - \sqrt{(x + \alpha)^2 + \beta^2} - \sqrt{(x - \alpha)^2 + \beta^2} \quad (6)$$

and

$$H(x, y) = \frac{1}{2}y^2 + x^2 - \sqrt{(x + \alpha)^2 + \beta^2} - \sqrt{(x - \alpha)^2 + \beta^2}, \quad (7)$$

respectively.

The equilibria of Equation (5) can be determined by letting its right side be 0. Evidently, for the positions of the equilibria, $y = 0$. Given $\alpha = 0.3$, the variation of the potential energy function $V(x)$ with the dimensionless displacement x is depicted in Figure 2 at different values of β . As can be observed from Figure 2, the system shows multi-stable static characteristics such as mono-potential wells, double-potential wells, and triple-potential wells at $\beta = 0.85$, $\beta = 0.5$ and $\beta = 0.1$, respectively. It demonstrates that the numbers of equilibria and the potential wells for the unperturbed system (5) depend on the values of the geometric parameters α and β .

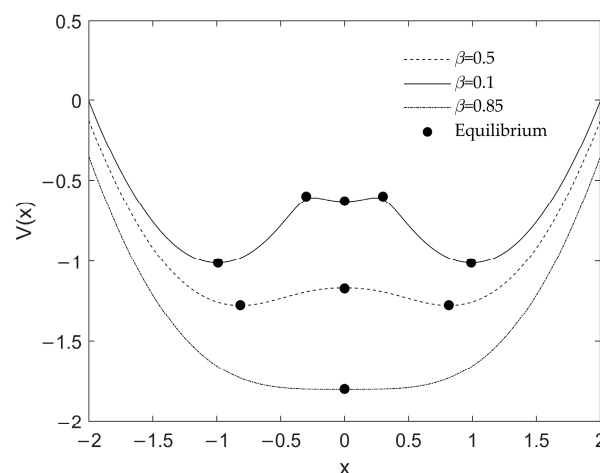


Figure 2. Potential energy function versus x at $\alpha = 0.3$ and various values of β .

Because there are two different irrationally nonlinear terms in the unperturbed system (5), the horizontal coordinate positions of the equilibria cannot be written in the form of explicit functions of the dimensionless parameters α and β , implying the difficulty of achieving analytical conditions of static bifurcation. Consequently, the cell-mapping method is used to numerically classify the regions under the same numbers of equilibria and the same nature of the system's potential wells (5) in the parameter plane α —, comprising the 499×499 array of parameter-condition points in the range $0 < \alpha < 1$ and $0 < \beta < 1$. On this basis, the details for the static bifurcation diagram and the corresponding phase portraits are described in Figure 3. In region I, there is a single equilibrium of the system (5), which is the origin as well as the center of the mono-potential well. In region II, there are three equilibria and double-potential wells among which the symmetric non-trivial equilibria are the potential-well centers surrounded by homoclinic orbits, and the origin is the saddle point. In region III, there are five equilibria and triple-potential wells in which the origin is a center surrounded by heteroclinic orbits crossing two non-trivial saddle points, and the other non-trivial equilibria are a pair of centers of the symmetric wells. In

the nondimensional system (3) when $f = 0$, the centers will become stable equilibria as $\zeta > 0$. This implies different stable equilibrium positions. In this case, the multistability of the system (3) will become apparent due to the limit points. However, it is unusable in the engineering applications of the oscillator such as vibration isolation and energy harvesting as the multistability will not lead to an increase in the displacement of the oscillator. For the practical applications of the oscillator, the multistability phenomenon that we focus on is the bistability within one potential well, as it can trigger a higher-amplitude response in a broad frequency band. Under the condition of three potential wells and $\alpha = 0.3$, the structural parameter β ranges from 0 to 0.22, which is too small and impractical for the engineering applications of the oscillator [3,4,10]. Therefore, in the following parts of this study, by fixing the value of β at 0.85 and 0.5, respectively, the cases of mono- and double-potential wells are the main focus.

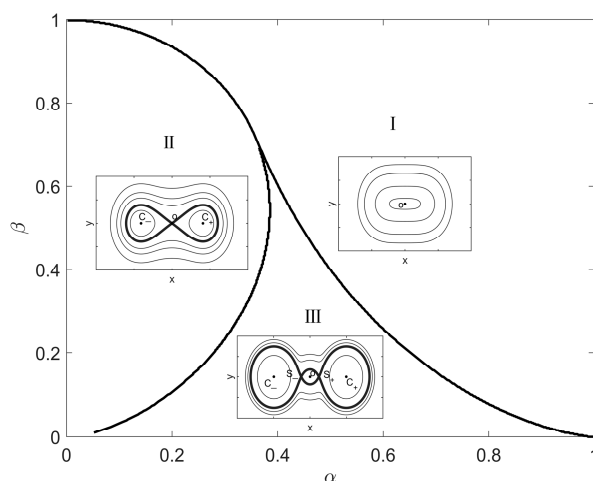


Figure 3. Bifurcation diagram of the unperturbed system (5).

3. Analysis of Resonant Responses

3.1. Resonant Responses in the Case of the Mono-Potential Well

To analyze the resonant responses of the non-dimensional system (3) in the vicinity of the center of the single-potential well, we first expand its fractional terms of x in the Taylor’s series in the neighborhood of the origin, thus obtaining

$$\ddot{x} + 2\zeta\dot{x} + \tilde{\omega}^2x + P_3x^3 = f \cos \omega T \tag{8}$$

where

$$\tilde{\omega} = \sqrt{2 - \frac{2\beta^2}{(\alpha^2 + \beta^2)^{\frac{3}{2}}}}, P_3 = \frac{\beta^2(\beta^2 - 4\alpha^2)}{(\alpha^2 + \beta^2)^{\frac{7}{2}}}. \tag{9}$$

In Equation (9), the parameter $\tilde{\omega}$ denotes the natural frequency of the horizontal-direction vibration, which is determined by the values of the two dimensionless structural parameters α and β .

We employ the method of multiple scales (MMS) to achieve the approximation of the analytical solutions of the system (8) under harmonic resonance. Bringing a small parameter ϵ satisfying $0 < \epsilon \ll 1$ into the system (8) to rescale the parameters ζ , ω and f , time variable T and the nondimensional displacement x in Equation (8) as follows,

$$\begin{aligned} \zeta &= \epsilon\tilde{\zeta}, \omega^2 = \tilde{\omega}^2 + \epsilon\sigma, f = \epsilon^2\tilde{f}, \\ x &= \epsilon x_1 + \epsilon^2 x_2 + \epsilon^3 x_3 + \dots, \\ T_i &= \epsilon^i T, D_i = \frac{\partial}{\partial T_i}, \frac{d}{dT} = D_0 + \epsilon D_1 + \epsilon^2 D_2 + \dots, (i = 1, 2, 3 \dots) \end{aligned} \tag{10}$$

and then separating the coefficients of ε , ε^2 and ε^3 leads to the equations below:

$$\varepsilon : D_0^2 x_1 + \omega^2 x_1 = 0, \quad (11)$$

$$\varepsilon^2 : D_0^2 x_2 + \omega^2 x_2 = \sigma x_1 - 2D_1 D_0 x_1 - 2\tilde{\xi} D_0 x_1 + \tilde{f} \cos \omega T, \quad (12)$$

and

$$\varepsilon^3 : D_0^2 x_3 + \omega^2 x_3 = -D_1^2 x_1 - P_3 x_1^3 - 2\tilde{\xi} D_1 x_1 + \sigma x_2 - 2D_2 D_1 x_1 - 2D_1 D_0 x_2 - 2\tilde{\xi} D_0 x_2. \quad (13)$$

Equation (11) is much like a free-vibration dynamical system [30–33]; thus, its solution can be set as

$$x_1 = A(T_1, T_2)e^{i\omega T_0} + \bar{A}(T_1, T_2)e^{-i\omega T_0} \quad (14)$$

where

$$A(T_1, T_2) = \frac{a(T_1, T_2)}{2} e^{i\varphi(T_1, T_2)}. \quad (15)$$

By substituting the above solution x_1 into Equation (12) and eliminating its secular terms, we get

$$D_1 A = -\tilde{\xi} A - \frac{i\sigma A}{2\omega} - \frac{i\tilde{f}}{4\omega}, \quad x_2 = 0. \quad (16)$$

Similarly, substituting Equations (14)–(16) into Equation (13) and eliminating its secular terms results in

$$D_2 A = -\frac{i\tilde{\xi}^2 A}{2\omega} + \frac{\tilde{f}\tilde{\xi}}{8\omega^2} - \frac{i\sigma^2 A}{8\omega^3} - \frac{i\sigma\tilde{f}}{16\omega^3} + \frac{3iP_3 A^2 \bar{A}}{2\omega}. \quad (17)$$

For the resonant solutions of the system (3), there is

$$\dot{A} \approx D_0 A + \varepsilon D_1 A + \varepsilon^2 D_2 A. \quad (18)$$

As can be derived from Equations (10), (14) and (15), the amplitude of the resonant solution x can be given by $\hat{a} = \varepsilon a$. By substituting Equations (16) and (17) into Equation (18), we can express the amplitude a and the phase angle φ by the original nondimensional parameters of the system (3), as follows:

$$\begin{aligned} \dot{\hat{a}} &= \frac{\tilde{\xi} f}{4\omega^2} \cos \varphi - \frac{(5\omega^2 - \tilde{\omega}^2) f}{8\omega^3} \sin \varphi - \tilde{\xi} \hat{a}, \\ \hat{a} \dot{\varphi} &= -\frac{(5\omega^2 - \tilde{\omega}^2) f}{8\omega^3} \cos \varphi - \frac{\tilde{\xi} f}{4\omega^2} \sin \varphi - \frac{((5\omega^2 - \tilde{\omega}^2)(\omega^2 - \tilde{\omega}^2) + 4\omega^2 \tilde{\xi}^2) \hat{a}}{8\omega^3} + \frac{3P_3 \hat{a}^3}{8\omega}. \end{aligned} \quad (19)$$

Letting $\dot{\hat{a}} = 0$ and $\dot{\varphi} = 0$ yield

$$(5\omega^2 - \tilde{\omega}^2)^2 f^2 + 4\omega^2 f^2 \tilde{\xi}^2 = 64\omega^6 \tilde{\xi}^2 \hat{a}^2 + [3P_3 \omega^2 \hat{a}^3 - ((5\omega^2 - \tilde{\omega}^2)(\omega^2 - \tilde{\omega}^2) + 4\omega^2 \tilde{\xi}^2) \hat{a}]^2. \quad (20)$$

The amplitude of the resonant solution, i.e., \hat{a} , can be solved using the above equation.

Based on the Jacobi matrix of Equation (19), the following characteristic equation can be derived to decide the stability of the resonant solution x :

$$\lambda^2 + 2\tilde{\xi}\lambda + [\tilde{\xi}^2 + (\frac{4\tilde{\xi}^2 + 4(\omega^2 - \tilde{\omega}^2) - 9P_3 \hat{a}^2}{8\omega} + \frac{(\omega^2 - \tilde{\omega}^2)^2}{8\omega^3}) (\frac{4\tilde{\xi}^2 + 4(\omega^2 - \tilde{\omega}^2) - 3P_3 \hat{a}^2}{8\omega} + \frac{(\omega^2 - \tilde{\omega}^2)^2}{8\omega^3})] = 0. \quad (21)$$

Due to the presence of the term $2\tilde{\xi}\lambda$ in Equation (21), there will be no purely imaginary solutions of the above equation as the other terms will be real numbers. Thus, the stability of the periodic solution will change only if $\lambda = 0$, i.e.,

$$\zeta^2 + \left(\frac{4\zeta^2 + 4(\omega^2 - \tilde{\omega}^2) - 9P_3\hat{a}^2}{8\omega} + \frac{(\omega^2 - \tilde{\omega}^2)^2}{8\omega^3} \right) \left(\frac{4\zeta^2 + 4(\omega^2 - \tilde{\omega}^2) - 3P_3\hat{a}^2}{8\omega} + \frac{(\omega^2 - \tilde{\omega}^2)^2}{8\omega^3} \right) = 0. \tag{22}$$

Combining Equations (20) and (21), the critical conditions for the saddle-node (SN) bifurcation, namely, the SN bifurcation points in system–parameter planes, can be determined. For each stable periodic solution, the solutions of its corresponding characteristic Equation (21) will both have negative real parts, while for an unstable periodic solution, there will be positive real parts in the solutions of its corresponding characteristic Equation (21).

Figure 4 is presented to show the variation of the amplitude of the resonant response with the dimensionless excitation level and frequency. The solution branches are divided into stable and unstable ones at SN bifurcation points denoted by small purple circles in Figure 4. The solid and dashed curves represent the stable and unstable solution branches, respectively. As denoted by the crosses in Figure 4, the numerical simulations for the stable responses of the ordinary differential Equation (4) are achieved via the fourth-order Runge-Kutta method, i.e., the software package ODE45 of MATLAB (2018a). Evidently, these are in agreement with the analytic results, herein validating the accuracy of the analysis.

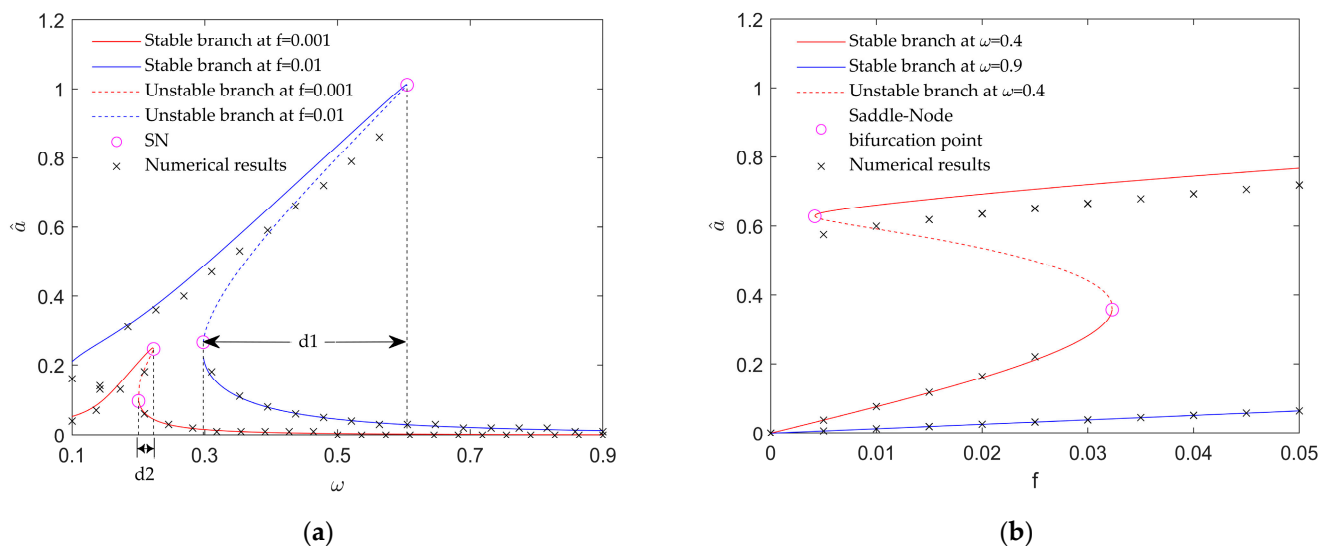


Figure 4. Variation of the resonant solutions around the origin with dimensionless excitation, in which $\beta = 0.85$ and $\zeta = 0.01$: (a) the amplitude frequency response at two different values of f , and (b) the amplitude of the resonant solution versus the dimensionless excitation level f at different values of ω .

As illustrated in Figure 4a, as ω rises, the two solution branches both bend to the right, showing stiffness-hardening characteristics and yielding bistable periodic responses in the vicinity of the origin. Similar frequency spectrums have been found in much of the literature on nonlinear vibrating systems [34–37], as they constitute an effective way to show the usable frequency range for higher-amplitude periodic responses. It can be observed in Figure 4a that there are two frequency bands $d1$ and $d2$ for $f = 0.001$ and $f = 0.01$, respectively, in which the bistable responses occur in the system. It demonstrates that increasing the dimensionless excitation level f can broaden the bandwidth for bistability, so that the resonant peak grows higher for a larger f . At $f = 0.01$, there are two critical points for SN bifurcation: with the rise of the excitation frequency ω from 0.57, the phenomenon jump occurs from the upper response branch to the lower one (see the solid blue curves), which is unfavorable for the utilization of the oscillator in energy collection and vibration isolation. For instance, at the blue solution branches for $f = 0.01$, the cases of $\omega = 0.4$ and $\omega = 0.9$ represent typical values within and out of the ranges of ω between its critical values

for the two SN bifurcation points, respectively, the situations are totally different. For the former, there are bistable periodic responses with much higher amplitudes, while for the latter, there is a single response with a low amplitude.

Figure 4b presents the variation of the amplitude of the periodic response with f when the value of the dimensionless excitation frequency is fixed at ω at $\omega = 0.9$ and $\omega = 0.4$, successively. Obviously, the response at $\omega = 0.9$ is monostable with a low amplitude. Comparatively, at $\omega = 0.4$, the amplitude of the periodic response is far higher, and the SN bifurcations of the periodic solution can also be observed, indicating that jump between bistable solution branches can stem from the growth of the excitation level f . If f does not exceed its critical value at the left SN bifurcation point, the solution branch will be monostable with a low amplitude. Otherwise, a higher-amplitude response branch will arise and coexist with the previous branch. When f exceeds the critical value at the right SN bifurcation point, the lower-amplitude response vanishes; the final response of the system (3) will definitely snap through to the higher-amplitude response branch. From then on, the higher-amplitude response will be monostable, which is desirable for the application of the structure.

3.2. Periodic Responses in the Case of Double Potential Wells

In this section, the periodic responses of the system (3) are analyzed under the circumstance of double-potential wells and the primary resonance in which its unperturbed system has two nontrivial centers and a trivial saddle point. Based upon the bifurcation diagram in Figure 3 and the unperturbed orbits of the region II, there are not only close loops within each potential well but also within the ones outside of the homoclinic orbits surrounding the double-potential wells. Hence, in this system (3), there may be intra-well periodic responses as well as inter-well responses, which are discussed separately.

3.2.1. Periodic Responses near Each Nontrivial Equilibrium Point

To begin with, we focus on the intra-well periodic responses. Because the intra-well attractors are in the vicinity of the nontrivial centers $C(\pm x_c, 0)$, we set

$$x = \pm x_c + \hat{x} \tag{23}$$

to rewrite the non-dimensional system (3) as

$$\ddot{\hat{x}} + 2\zeta\dot{\hat{x}} + 2\hat{x} - \frac{\pm x_c + \hat{x} + \alpha}{\sqrt{(\pm x_c + \hat{x} + \alpha)^2 + \beta^2}} - \frac{\pm x_c + \hat{x} - \alpha}{\sqrt{(\pm x_c + \hat{x} - \alpha)^2 + \beta^2}} = f \cos \omega T. \tag{24}$$

Similar to the last section, expanding its fractional terms of x into Taylor’s series, Equation (24) becomes

$$\ddot{\hat{x}} + 2\zeta\dot{\hat{x}} + \hat{\omega}^2\hat{x} \pm Q_2\hat{x}^2 + Q_3\hat{x}^3 = f \cos \omega T \tag{25}$$

where

$$\begin{aligned} \hat{\omega}^2 &= 2 - \frac{\beta^2}{((x_c + \alpha)^2 + \beta^2)^{\frac{3}{2}}} - \frac{\beta^2}{((x_c - \alpha)^2 + \beta^2)^{\frac{3}{2}}}, \\ Q_2 &= \frac{3(x_c + \alpha)\beta^2}{2((x_c + \alpha)^2 + \beta^2)^{\frac{5}{2}}} + \frac{3(x_c - \alpha)\beta^2}{2((x_c - \alpha)^2 + \beta^2)^{\frac{5}{2}}}, \\ Q_3 &= \frac{\beta^4 - (3x_c\beta + 2\alpha\beta)^2}{2((x_c + \alpha)^2 + \beta^2)^{\frac{7}{2}}} + \frac{\beta^4 - (3x_c\beta - 2\alpha\beta)^2}{2((x_c - \alpha)^2 + \beta^2)^{\frac{7}{2}}}. \end{aligned} \tag{26}$$

In the above equation, the parameter $\hat{\omega}$ denotes the natural frequency of the system (3) with double-potential wells.

Identically to the last section, MMS is utilized to obtain the approximation of the resonant solutions for the system (25). By rewriting ω , the displacement \hat{x} , T and differential operators as

$$\omega^2 = \hat{\omega}^2 + \varepsilon\sigma, \hat{x} = \varepsilon\hat{x}_1 + \varepsilon^2\hat{x}_2 + \varepsilon^3\hat{x}_3 + \dots, T_i = \varepsilon^i T, \frac{d}{dT} = D_0 + \varepsilon D_1 + \varepsilon^2 D_2 + \dots, D_i = \frac{\partial}{\partial T_i}. (i = 1, 2, 3 \dots), \tag{27}$$

and comparing the coefficients of $\varepsilon, \varepsilon^2$ and ε^3 of the system (25), we obtain

$$\varepsilon : D_0^2 \hat{x}_1 + \omega^2 \hat{x}_1 = 0, \tag{28}$$

$$\varepsilon^2 : D_0^2 \hat{x}_2 + \omega^2 \hat{x}_2 = -2\tilde{\xi} D_0 \hat{x}_1 - 2D_1 D_0 \hat{x}_1 \mp Q_2 \hat{x}_1^2 + \sigma \hat{x}_1 + \tilde{f} \cos \omega T, \tag{29}$$

and

$$\varepsilon^3 : D_0^2 \hat{x}_3 + \omega^2 \hat{x}_3 = -D_1^2 \hat{x}_1 - 2\tilde{\xi} D_1 \hat{x}_2 - C_3 \hat{x}_1^3 \mp 2C_2 \hat{x}_1 \hat{x}_2 + \sigma \hat{x}_2 - 2D_2 D_0 \hat{x}_1 - 2D_1 D_0 \hat{x}_2 - 2\tilde{\xi} D_0 \hat{x}_2. \tag{30}$$

The complete solution for Equation (28) can be solved, given by

$$\hat{x}_1 = B(T_1, T_2)e^{i\omega T_0} + \bar{B}(T_1, T_2)e^{-i\omega T_0} \tag{31}$$

where

$$B(T_1, T_2) = \frac{b(T_1, T_2)}{2} e^{i\psi(T_1, T_2)}. \tag{32}$$

Thus, the resonant solution x can be rewritten approximately as

$$x = \pm x_c + \hat{b} \cos(\omega T_0 + \psi). \tag{33}$$

Its amplitude can be written as

$$\hat{b} = \varepsilon b. \tag{34}$$

Substituting the solution \hat{x}_1 , namely, Equations (31) and (32), into Equation (29) and eliminating the secular terms there results in

$$D_1 B = -\tilde{\xi} B - \frac{i\sigma B}{2\omega} - \frac{i\tilde{f}}{4\omega}, \tag{35}$$

and

$$\hat{x}_2 = \pm \frac{Q_2 B^2}{3\omega^2} e^{2i\omega T_0} \mp \frac{2Q_2 B \bar{B}}{\omega^2} + cc. \tag{36}$$

Afterward, substituting Equations (31), (35) and (36) into Equation (30) yields

$$D_2 B = \frac{(\tilde{\xi}\omega - i\sigma)\tilde{f}}{8\omega^3} - \frac{i(4\omega^2\tilde{\xi}^2 + \sigma^2)B}{8\omega^3} + \frac{i(9\omega^2 Q_3 - 10Q_2^2)B^2 \bar{B}}{6\omega^3}. \tag{37}$$

For Equation (32), we consider $\dot{B} \approx D_0 B + \varepsilon D_1 B + \varepsilon^2 D_2 B$ and Equations (34), (35) and (37), and we return the concerning parameters into the ones in the original system (3) simultaneously in order to acquire the following equation for the level and phase angle of the resonant solution x :

$$\begin{aligned} \dot{\hat{b}} &= -\frac{(3\omega^2 - \hat{\omega}^2)f}{4\omega^3} \sin \psi + \frac{\tilde{\xi}f}{4\omega^2} \cos \psi - \tilde{\xi}\hat{b}, \\ \hat{b}\dot{\psi} &= -\frac{(3\omega^2 - \hat{\omega}^2)f}{4\omega^3} \cos \psi - \frac{\tilde{\xi}f}{4\omega^2} \sin \psi - \frac{(4\omega^3\tilde{\xi}^2 + (4\omega^3 + 1)(\omega^2 - \hat{\omega}^2))\hat{b}}{8\omega^3} + \frac{(9\omega^2 Q_3 - 10Q_2^2)\hat{b}^3}{24\omega^3}. \end{aligned} \tag{38}$$

Supposing the right side of the above equation be zero and eliminating its trigonometric terms, the equation for the resonant solution amplitude is obtained as follows:

$$\left(\frac{f}{2\omega} + \frac{\omega^2 - \hat{\omega}^2}{4\omega^3}\right)^2 + \left(\frac{\tilde{\xi}f}{4\omega^2}\right)^2 = \tilde{\xi}^2 \hat{b}^2 + \left(\frac{\omega^2 - \hat{\omega}^2}{2}\right)\hat{b} + \frac{\tilde{\xi}^2}{2\omega}\hat{b} + \frac{(\omega^2 - \hat{\omega}^2)^2}{8\omega^3}\hat{b} + \frac{(10Q_2^2 - 9\omega^2 Q_3)}{24\omega^3}\hat{b}^3. \tag{39}$$

Based on Equations (38) and (39), the following characteristic equation is obtained for determining the stability of the corresponding periodic solution:

$$\lambda^2 + 2\zeta\lambda + \Gamma = 0 \tag{40}$$

where

$$\Gamma = \frac{1}{4}(\omega^2 - \hat{\omega}^2 + \frac{4\zeta^2 - 9Q_3b^2}{4\omega} + \frac{(\omega^2 - \hat{\omega}^2) + 10Q_2^2b^2}{4\omega^3})(\omega^2 - \hat{\omega}^2 + \frac{4\zeta^2 - 3Q_3b^2}{4\omega} + \frac{3(\omega^2 - \hat{\omega}^2) + 10Q_2^2b^2}{12\omega^3}). \tag{41}$$

Due to the term $2\zeta\lambda$, Equation (40) has no purely imaginary solutions as Γ is always a real number. Accordingly, the stability of the resonant solution will change only if there is a simple zero solution for it. Combining Equation (39) and $\Gamma = 0$, we can determine the critical conditions of the two dimensionless parameters ω and f for the SN bifurcation of the resonant solution.

Because the intra-well responses surrounding the symmetric well centers are symmetric as well, the response amplitudes within different wells are the same. The variation of the responses in the vicinity of the center $C_+(x_c, 0)$ can herein represent the intra-well responses within both potential wells. Figure 4 displays the roles of the excitation parameters in affecting the steady-state behaviors for $\zeta = 0.01$ and $\alpha = 0.5$.

In contrast to Figure 4a, it can be observed in Figure 5a that with the rise of ω , the periodic-solution branch for $f = 0.01$ bends to the left, thus showing soft-spring characteristics and triggering bistable resonant responses in the neighborhood of each nontrivial equilibrium (see the frequency band for the resonant responses denoted by d in Figure 4a). Decreasing ω from 1.05 may cause the upper solution branch to jump down to the lower branch, which is ascribed to the SN bifurcations of the intra-well periodic solution. For instance, for $f = 0.01$ and $\omega = 0.9$, two periodic responses coexist; the amplitude of the periodic response in the upper solution branch is much higher than the one in the lower solution branch. As can be calculated from Equation (26) and observed from the red solution branch of Figure 4a, the natural frequency $\hat{\omega} \approx 1.09$. In Figure 4a, the numerical results coincide well with the analytical results, except for the left side of the SN bifurcation points. This discrepancy can be ascribed to the restrictions of MMS, namely, MMS does not work well under the condition that the excitation amplitude ranges beyond the neighborhood of the natural frequency $\hat{\omega}$, and when the response amplitude is large.

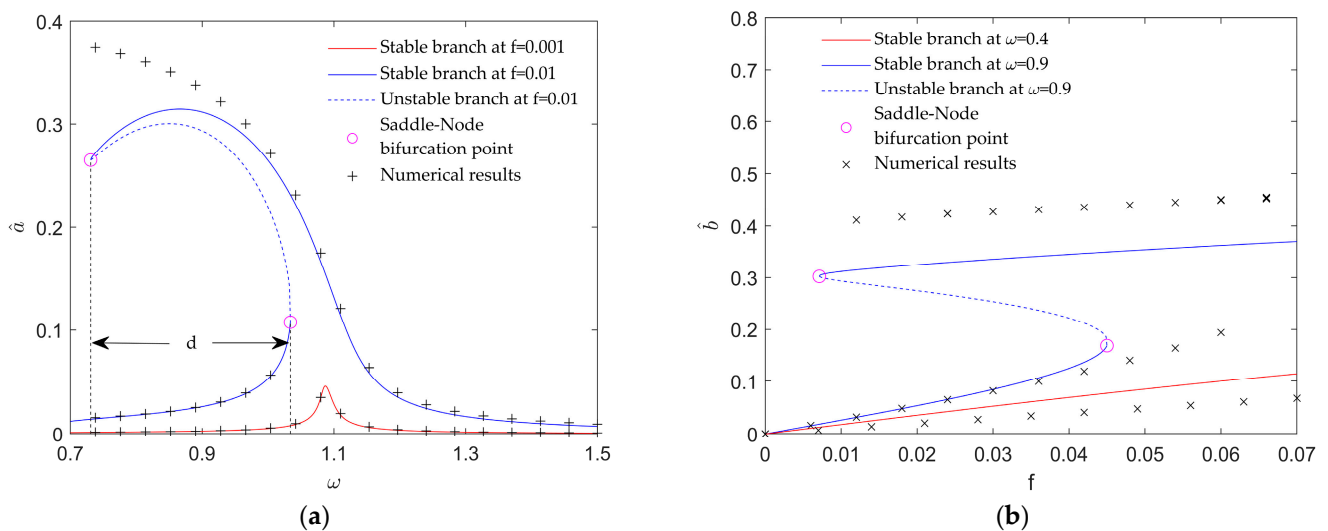


Figure 5. Variations of the resonant behaviors in the vicinity of each nontrivial equilibrium with dimensionless excitation when $\beta = 0.5$ and $\zeta = 0.01$: (a) the amplitude frequency responses at different values of f , and (b) the amplitude of the resonant response versus f at different values of ω .

In comparison to the resonant responses in the case of mono-potential wells, the frequency band for achieving higher-amplitude intra-well responses in double-potential wells is totally different. It is because there is a quite difference between the natural frequencies for the cases of mono-potential wells and double-potential wells: 0.19 and 1.09, respectively. For example, $\omega = 0.9$ is in the frequency band of the latter, but out of the frequency band of the former: $\omega = 0.4$ is just the opposite.

Therefore, the dimensionless excitation frequency ω in Figure 5b is given the same values in Figure 4b, namely, $\omega = 0.9$ and $\omega = 0.4$ (see the red and blue curves). Clearly, the amplitudes of the responses for $\omega = 0.9$ are higher than the ones for $\omega = 0.4$. We can also observe two SN bifurcation points at $\omega = 0.9$. Between the critical values for f of the SN bifurcation points, the two stable periodic response coexist. When $\omega = 0.9$ and f exceeds its critical values for the right SN bifurcation points, the periodic response in the upper solution branch becomes the only stable attractor of the system (3) with an amplitude that is far beyond the amplitude of the periodic response at $\omega = 0.4$, which is favorable for the engineering applications of the irrationally nonlinear structure.

When comparing Figures 4a and 5a, it can be seen that the adjustment of the parameter β , namely, the vertical distance between the oscillator and the fixed pin, can change the stiffness softening/hardening characteristics and the usable frequency band of the oscillatory system.

3.2.2. Inter-Well Periodic Solutions

Resonant solutions around the origin are totally different from the ones around the non-trivial centers because the former is beyond the potential wells as well as the homoclinic orbits surrounding the well centers. It is evident that this type of resonant response is called the inter-well response because it has an absolutely larger amplitude than the intra-well ones. On account of the restriction of MMS, it can work well only if discussed responses are in the neighborhood of the well centers; this method is useless for the analysis of the inter-well responses. Accordingly, the average method [15] is employed in this section.

We can rewrite the inter-well resonant solution x by the slowing-varying level a_0 and frequency ω in the following form:

$$x = a_0 \cos(\omega T + \theta), \dot{x} = -a_0 \omega \sin(\omega T + \theta). \tag{42}$$

Correspondingly, the non-dimensional system (3) can be rewritten as

$$\dot{a}_0 \cos(\omega T + \theta) - a_0 \sin(\omega T + \theta) \dot{\theta} = 0, \dot{a}_0 \sin(\omega T + \theta) + a_0 \cos(\omega T + \theta) \dot{\theta} = \frac{1}{\omega} E(a_0, \theta, T) \tag{43}$$

where

$$E(a_0, \theta, T) = 2a_0 \omega \xi \sin(\omega T + \theta) + a_0(\omega^2 - \omega_0^2) \cos(\omega T + \theta) + f \cos \omega T + \frac{a_0 \cos(\omega T + \theta) + \alpha}{\sqrt{(a_0 \cos(\omega T + \theta) + \alpha)^2 + \beta^2}} + \frac{a_0 \cos(\omega T + \theta) - \alpha}{\sqrt{(a_0 \cos(\omega T + \theta) - \alpha)^2 + \beta^2}}. \tag{44}$$

According to Equations (42)–(44), the slowly varying parameters a_0 and ω are

$$\dot{a}_0 = -\frac{E}{\omega} \sin(\omega T + \theta), \dot{\theta} = -\frac{E}{a_0 \omega} \cos(\omega T + \theta). \tag{45}$$

Integrating Equation (45) over a whole period $[0, \frac{2\pi}{\omega}]$, setting its right side as zero and then eliminating its trigonometric terms yields

$$(2\pi \xi a \omega + E_1)^2 + (a\pi(\omega^2 - \omega_0^2) + E_2)^2 = \pi^2 f^2 \tag{46}$$

where

$$E_1 = \int_0^{2\pi} \left(\frac{a \cos T + \alpha}{\sqrt{(a \cos T + \alpha)^2 + \beta^2}} + \frac{a \cos T - \alpha}{\sqrt{(a \cos T - \alpha)^2 + \beta^2}} \right) \sin T dT, \quad E_2 = \int_0^{2\pi} \left(\frac{a \cos T + \alpha}{\sqrt{(a \cos T + \alpha)^2 + \beta^2}} + \frac{a \cos T - \alpha}{\sqrt{(a \cos T - \alpha)^2 + \beta^2}} \right) \cos T dT. \quad (47)$$

Whether the inter-well resonant solution is stable or not is decided by the real parts of the eigenvalues of the corresponding linearized average equation [15]. It follows from the corresponding derivation that the inter-well solution is asymptotically stable only if its amplitude exceeds the maximum of the horizontal abscissas of the homoclinic orbits, i.e., x_e and the following inequations are satisfied

$$\xi + \frac{1}{4\pi\omega} \left(\frac{\partial E_1}{\partial a_0} + \frac{E_1}{a_0} \right) > 0, \quad (2\pi\xi\omega + \frac{\partial E_1}{\partial a_0})(2\pi\xi\omega + \frac{E_1}{a_0}) + (\pi(\omega^2 - \omega_0^2) + \frac{\partial E_2}{\partial a_0})(\pi(\omega^2 - \omega_0^2) + \frac{E_2}{a_0}) > 0. \quad (48)$$

Thus, the SN bifurcation of this resonant solution will be triggered when

$$(2\pi\xi\omega + \frac{\partial E_1}{\partial a_0})(2\pi\xi\omega + \frac{E_1}{a_0}) + (\pi(\omega^2 - \omega_0^2) + \frac{\partial E_2}{\partial a_0})(\pi(\omega^2 - \omega_0^2) + \frac{E_2}{a_0}) = 0. \quad (49)$$

Because the intra-well responses have higher amplitudes at $\omega = 0.9$, we also considered the inter-well responses in this situation. The corresponding solution branches vary with the dimensionless excitation level f , as can be seen in Figure 6. The theoretical results and the numerical ones both show that is no inter-well periodic solution when f is very small. As the excitation amplitude exceeds its value at the bifurcating point, the inter-well periodic motion will occur. Evidently, it stems from the local bifurcation of this periodic solution. When comparing Figures 5b and 6, it is apparent that, as the dimensionless excitation amplitude f increases, multiple intra-well periodic attractors and one inter-well attractor may coexist, and the inter-well resonant response amplitude is the largest.

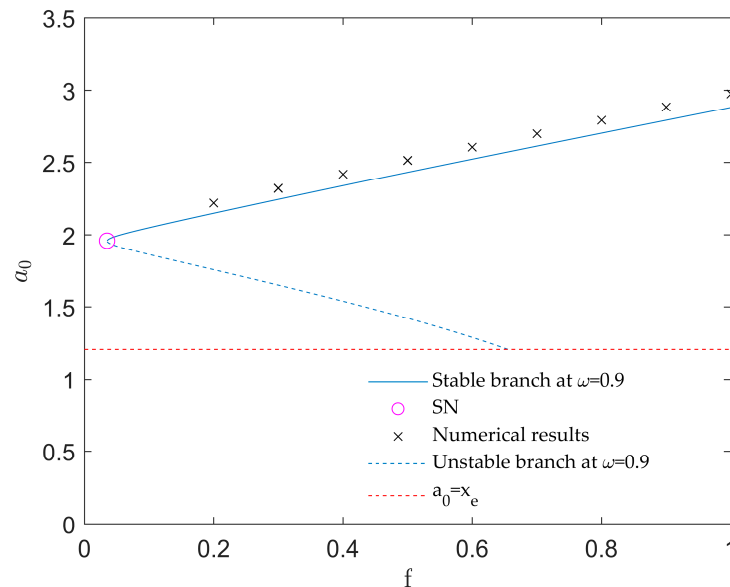


Figure 6. Amplitude variation of the inter-well resonant response with the rise of f .

4. Numerical Results

In the circumstance of multi-stability, the final dynamical response may be sensitive to the initial conditions. Thus, considering a single fixed initial condition is not enough to reveal the mechanism of the structural parameters and the excitation in affecting global dynamics. The disturbance of the initial conditions has to be taken into account, which suggests the demand for classifying the basins of attraction (BAs). For an arbitrary attractor, its basin of attraction (BA) indicates the union of all the initial states that cause it [29]. The cell-mapping method is employed to describe the Bas of the irrationally nonlinear oscillator

(3) on its initial-state plane $x(0) - y(0)$, which consists of the 301×151 array of initial-state points. Different attractors are drawn in different colors, while every attractor and its BA are marked in the same color. In this section, for $\alpha = 0.3$, we also focus on the cases of mono-potential wells and double-potential wells by fixing $\beta = 0.85$ and $\beta = 0.5$, respectively.

4.1. Attractors and Their BAs in the Case of Mono Potential Well

To remain consistent with the given excitation in Figure 4a, we first present the evolution of the attractors and their BAs with the rise of ω at $f = 0.01$, as can be seen in Figure 7. The two columns in Figure 7 show the phase maps of the attractors and their corresponding BAs, respectively. Initial conditions were chosen within the range $-1.0 \leq x(0) \leq 1.0$, $-0.6 \leq y(0) \leq 0.6$ which is sufficient to contain the stable periodic responses predicted in the last section.

In Figure 7(a1,a2), there is only a blue attractor as well as the blue initial plane, signaling the global stability of the periodic attractor from the upper solution branch of Figure 4a. As ω rises a bit to 0.31 (see Figure 7(b1,b2)), coexisting with it, a new attractor with a much lower amplitude appears which has a tiny BA. Hence, the lower-amplitude attractor is a rare attractor now. As ω keeps increasing, its BA becomes bigger and bigger, especially in the vicinity of the origin, showing its increasing accessibility. Specifically, at $\omega = 0.57$, the blue area in the initial plane is very small and is outside of the vicinity of the origin (see Figure 7(d2)), showing that the higher-amplitude attractor now turns into a rare and hidden attractor [30]. At $\omega = 0.6$, the BA for the higher amplitude vanishes, and the whole initial-condition plane becomes red (see Figure 7(e2)), implying that the final dynamic behavior of the system (3) will inevitably be the lower-amplitude response. The variation trends of the dynamical behaviors and their BAs with ω presented in Figure 7 match the analytical prediction of Figure 4a well, indicating that the analysis is valid.

According to Figure 7, for the achievement of higher-amplitude responses, the dimensionless frequency ω should be within the range (0.31, 0.57). When studying the change in the attractors and their BAs with f , we consider the value of ω in this range by fixing $\omega = 0.4$ (see Figure 8). As depicted in the left column of Figure 8, the periodic-response amplitude increases with f . In Figure 8(a1,a2), there is only one attractor and its BA. According to the analysis of Figure 4b, this periodic response is from the lower solution branch. Thus, we denote it in red. When f rises a bit to 0.0045, the red attractor loses its global stability and coexists with the blue attractor, showing bi-stability (see Figure 8(b1,b2)). The blue region representing the BA of the bigger attractor is very slim and not in the neighborhood of $O(0,0)$, so the higher-amplitude attractor here is a hidden attractor [30], and it is hard to achieve it. As f keeps rising, the BA of the bigger attractor becomes more and more visible. For $f = 0.028$, most of the area of the initial-state plane turns blue, and the red region is severely eroded. It means that the lower-amplitude attractor now becomes the hidden attractor. Meanwhile, the bigger attractor is more likely to occur as the final dynamical behavior. When $f = 0.029$, the red BA vanishes, and the initial-state plane is blue (see Figure 8(f2)), illustrating that the final response of the system (3) is the higher-amplitude response despite the initial conditions. It follows from Figures 3 and 8 that, with the rise of f , the sequences of the attractors and their basins qualitatively agree with the analytical prediction.

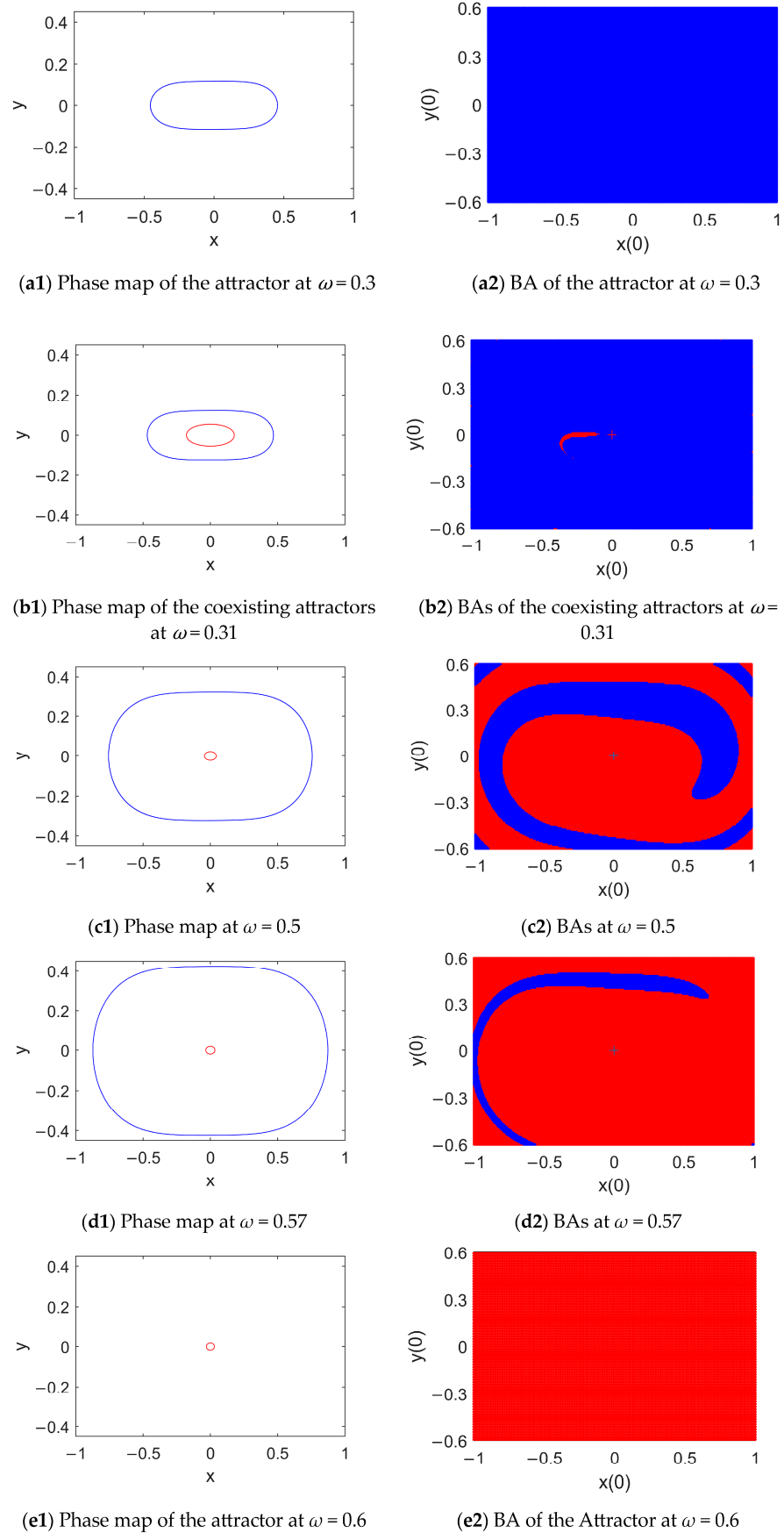


Figure 7. Changes of the attractors and their Bas with the rise of ω for $\beta = 0.85$ and $f = 0.01$; every attractor and its BA are marked in the same color.

4.2. Attractors and Their BAs in the Case of Double Potential Wells

For the case of double potential wells under $\alpha = 0.3$ and $\beta = 0.5$, Figures 5 and 6 show that at $\omega = 0.9$, the symmetric higher-amplitude intra-well periodic responses and lower-amplitude responses may coexist with an inter-well periodic response as f rises. Hence, in this section, by setting $\omega = 0.9$, we present the variation of coexisting responses and their BAs with the rise in f in the initial-state region $-2.0 \leq x(0) \leq 2.0$, $-2.5 \leq y(0) \leq 2.5$. As can be observed in Figure 9, the evolution of the attractors and the corresponding BAs is more complicated than the evolutions in Figures 7 and 8.

First, for $f = 0.002$, the symmetric periodic responses are of a pretty low amplitude, with BAs that are centrosymmetric as well (see Figure 9(a1,a2)). Also, the boundary separating their BAs is smooth. An arbitrary initial-state point selected near the point $C_+(x_c, 0)$ or $C_-(-x_c, 0)$ definitely induces the corresponding nontrivial equilibrium, meaning that they are locally stable. In contrast, a tiny perturbation in the initial condition in the neighborhood of the saddle point $O(0,0)$ can incur the phenomenon jump between the two symmetric attractors.

In addition to these two attractors, as f is increased to 0.01, two new symmetric intra-well periodic attractors with a higher amplitude occur (see in Figure 9(b1)). As can be observed from the nature of their BAs in Figure 9(b2), they are rare and hidden attractors. When f increases from 0.02 to 0.035 (see Figure 9(c1–e2)), the BAs of the lower-amplitude ones are steadily eroded. Meanwhile, the BAs of the higher-amplitude ones are broken into seriously fractal and discrete pieces, indicating the high initial-condition sensitivity of these dynamical behaviors even though they are not complex attractors.

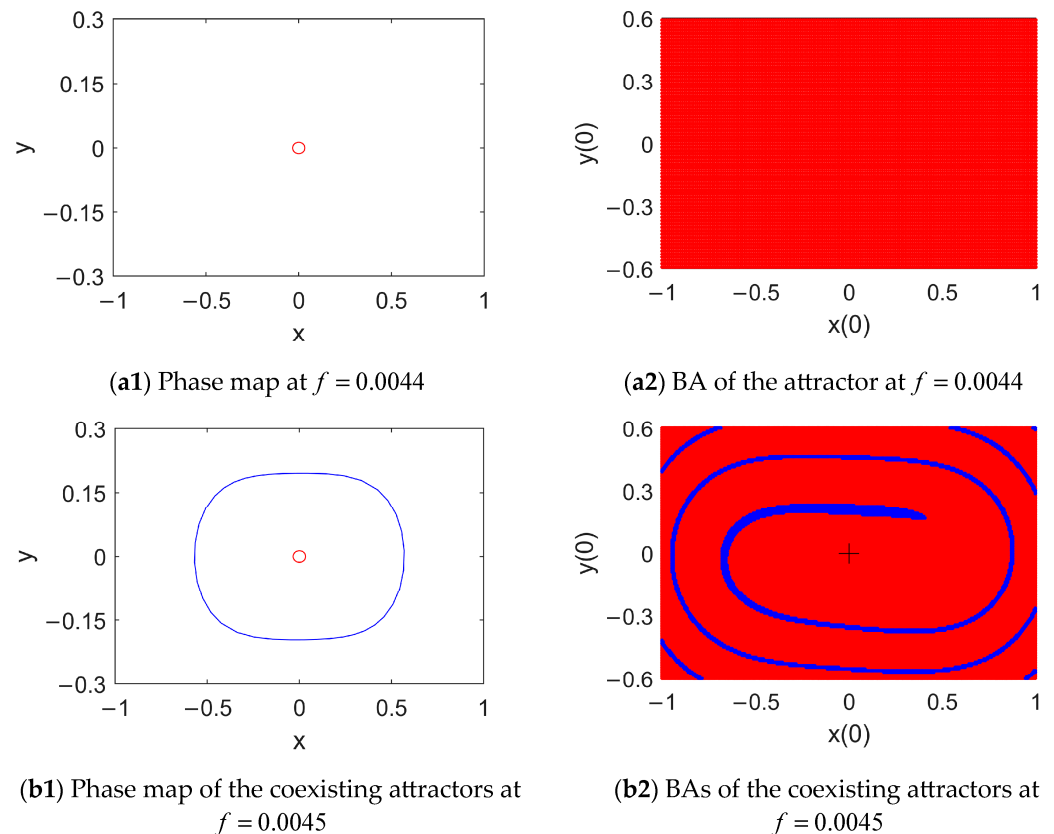


Figure 8. Cont.

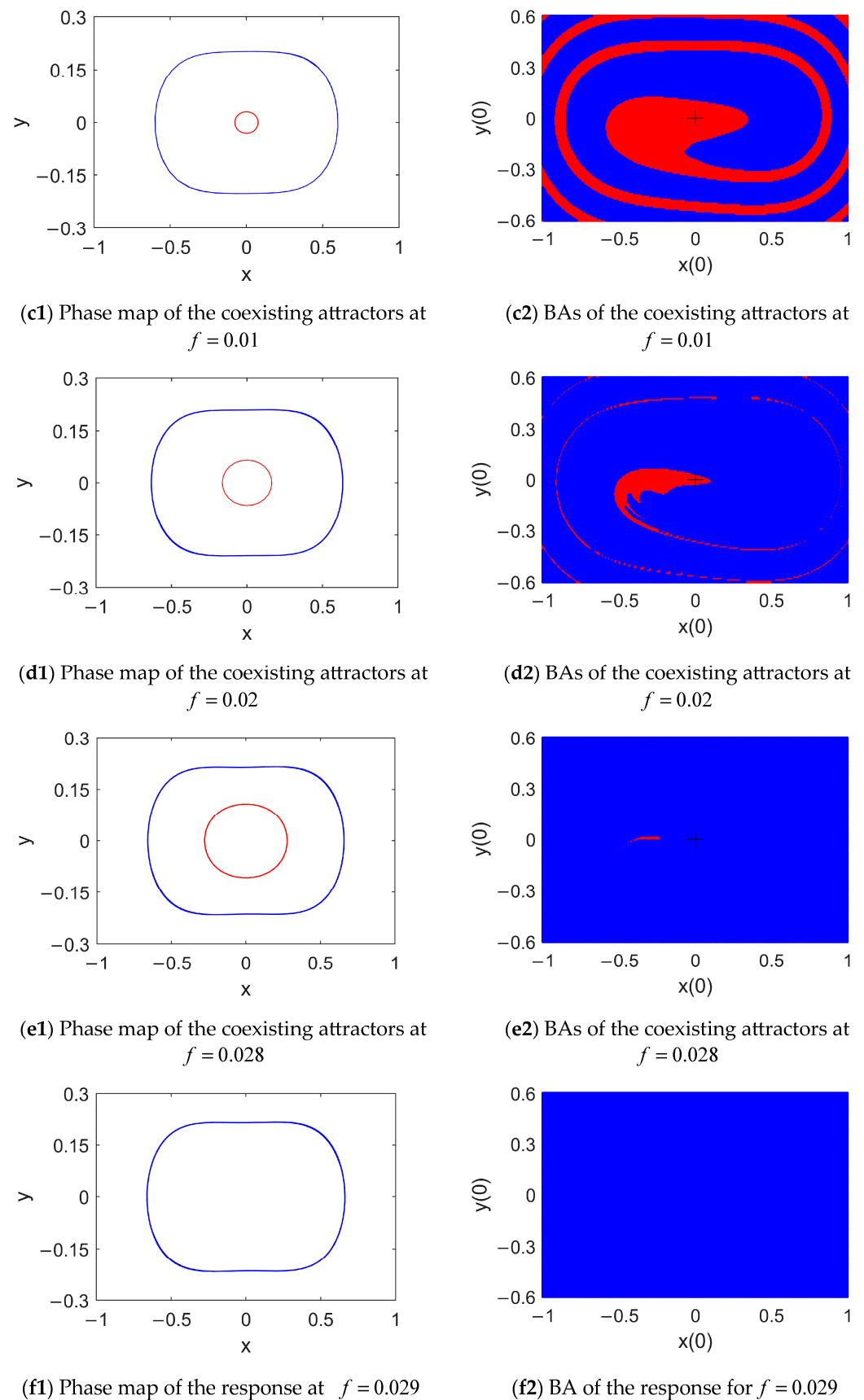


Figure 8. Change of attractors and their BAs with the rise of f at $\beta = 0.85$ and $\omega = 0.4$ where every attractor and its BA are marked in the same color.

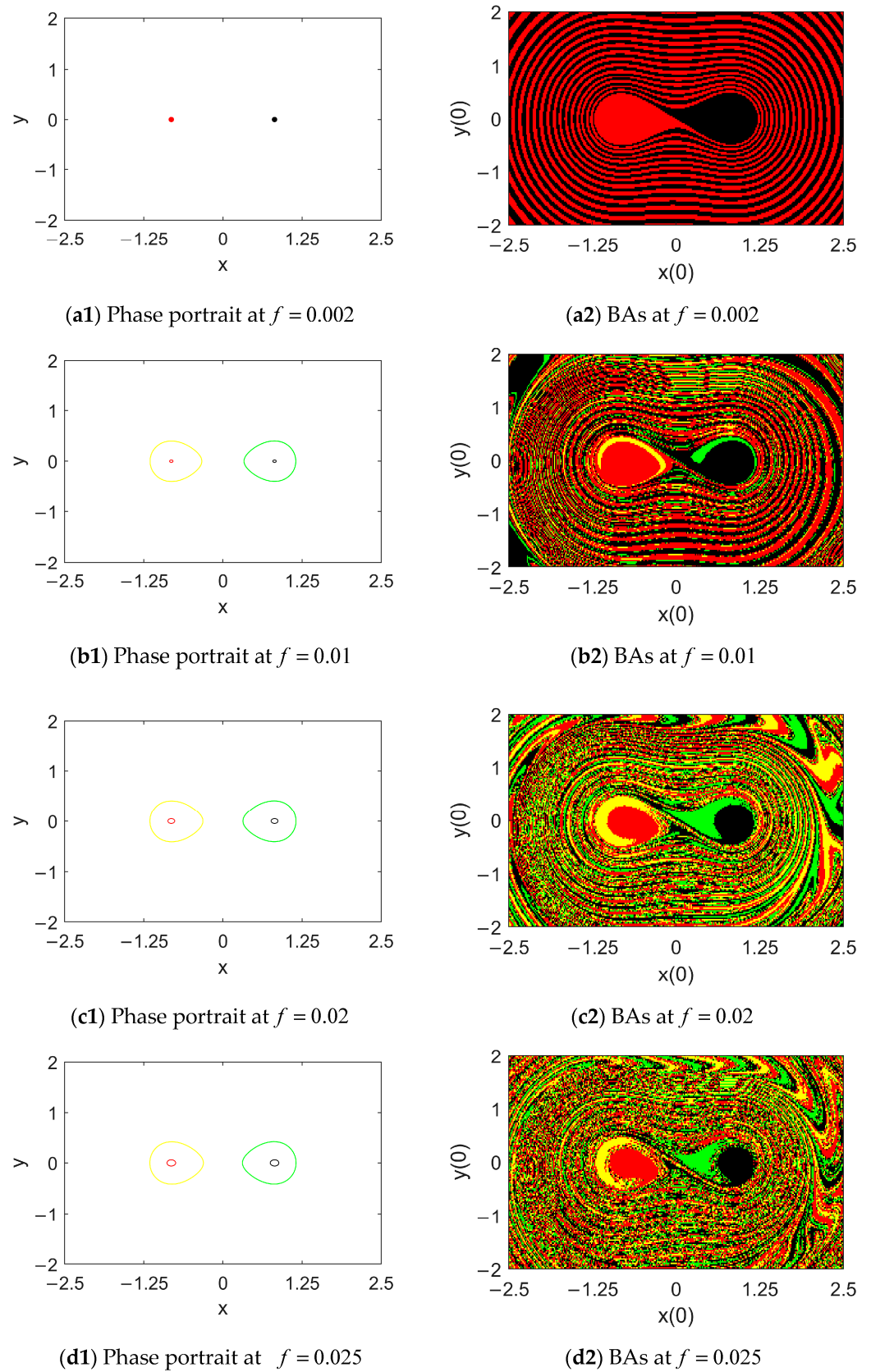


Figure 9. Cont.

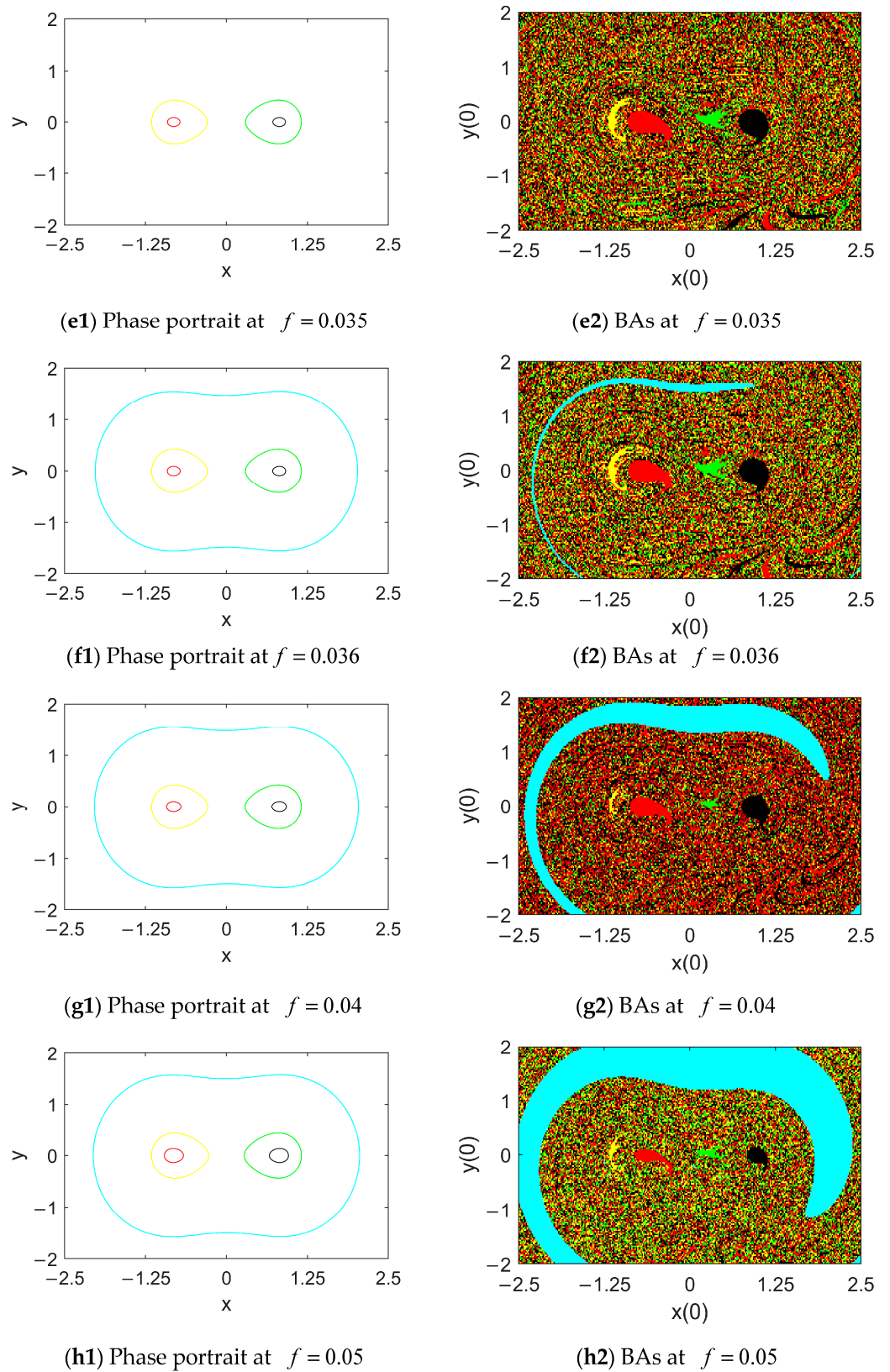


Figure 9. Cont.

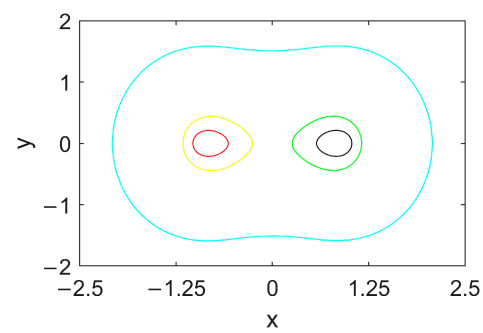
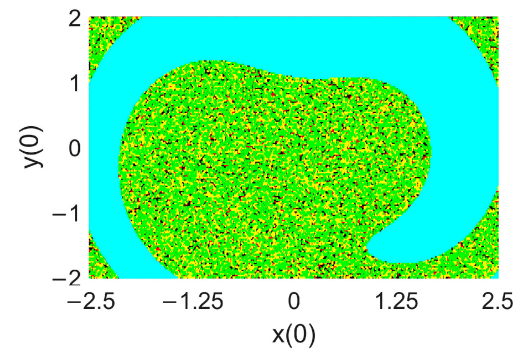
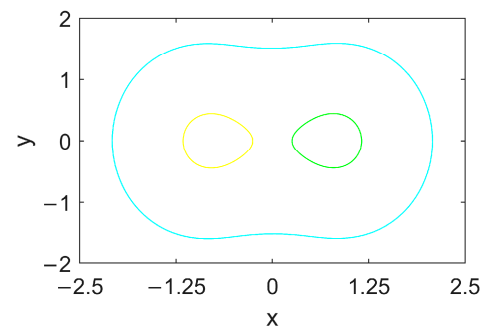
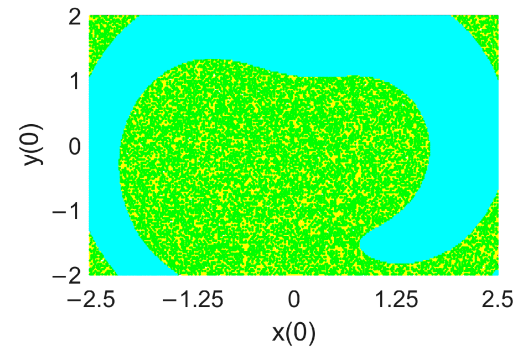
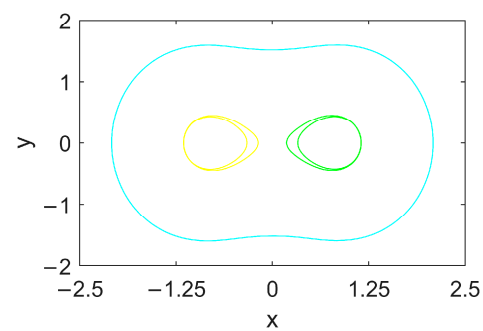
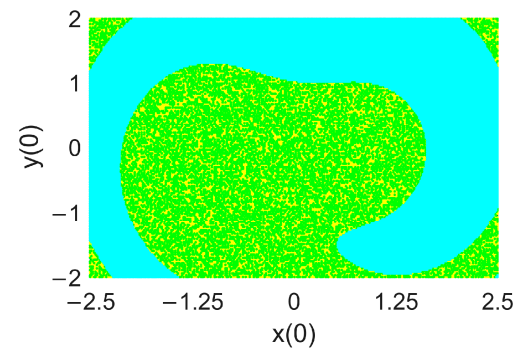
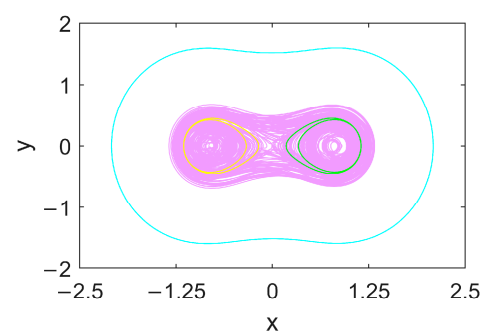
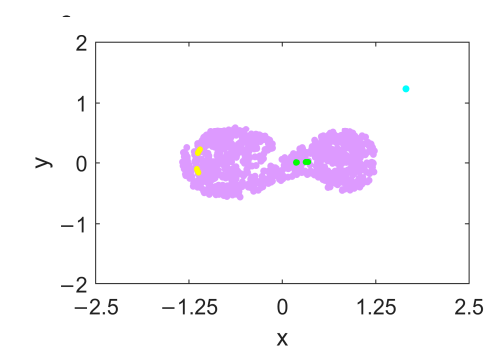
(i1) Phase portrait at $f = 0.064$ (i2) BAs at $f = 0.064$ (j1) Phase portrait at $f = 0.066$ (j2) BAs at $f = 0.066$ (k1) Phase portrait at $f = 0.073$ (k2) BAs at $f = 0.073$ (l1) Phase portrait at $f = 0.074$ (l2) Poincare map at $f = 0.074$

Figure 9. Cont.

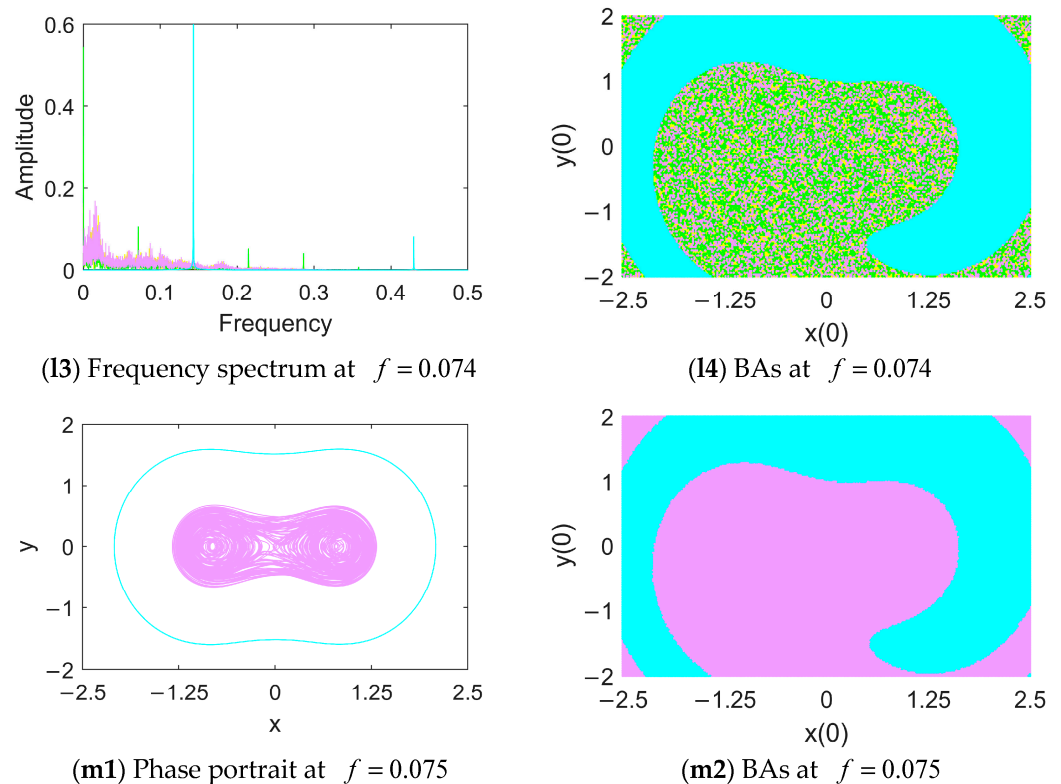


Figure 9. Variation of the coexisting responses and their BAs with the rise of f at $\beta = 0.5$ and $\omega = 0.9$, where every attractor and its BA are marked in the same color.

Then, as f rises to 0.036, an inter-well periodic response with a far higher amplitude will appear along with these intra-well resonant responses (see the light blue closed loop in Figure 9(f1)). Its occurrence verifies the prediction made in the last section. Because its tiny BA is far beyond the range of the vicinity of $O(0,0)$ (see Figure 9(f2)), it is a hidden and rare attractor.

Following this, as f increases from 0.036 to 0.064, the five periodic attractors still coexist (see Figure 9(g1–i2)). It can also be seen that the smallest attractors expand with the increase of f . The variation of their BAs also indicates that the BA of the inter-well resonant response steadily erodes the BAs of the intra-well responses. Note that its basin boundary is still smooth and without fractality. Comparatively, the BAs of all the intra-well attractors are intermingled with each other with seriously fractal natures.

Afterward, at $f = 0.066$, the smallest periodic attractors disappear (see Figure 9(j1)). The BAs of the other two intra-well responses are still in severe fractality, as illustrated in Figure 9(j2). As f reaches 0.073, these periodic responses become period-two responses, and their BAs remain nearly the same (see Figure 9(k1,k2)).

Furthermore, at $f = 0.074$, apart from the two period-two attractors and the inter-well periodic attractor, a new inter-well attractor appears. The corresponding phase portrait, Poincaré section and frequency spectrum signify that a chaotic attractor occurs in the system (3). As can be observed in Figure 9(l4), its BA is segmented into discontinuous and fractal pieces by the BAs of the intra-well complex attractors. It means the initial condition discontinuity of these complex responses, which is another kind of initial condition sensitivity, is different from the inherent initial condition sensitivity of chaos.

Finally, when f exceeds 0.075, there will be no intra-well responses, and the two inter-well attractors will coexist as depicted in Figure 9(m1). Specifically, the BA boundary of chaos is not fractal but glossy (see Figure 9(m2)), which is totally different from Figure 9(l4). It demonstrates the local stability and attraction of the two large-extent attractors. Specifically, the BA of chaos contains the vicinity of three equilibria, illustrating that chaos

has a higher probability of occurrence as the final behavior than the large-displacement resonant response.

5. Discussion

In this work, an irrationally nonlinear oscillator composed of two obliquely set-up elastic springs and a collar with a concentrated mass is considered. In the case of continuous nonlinearity and primary resonance, its global dynamics under different types of potential wells is discussed.

Its dynamical system is first constructed in order to derive its non-dimensional system. Based on its unperturbed system and the corresponding Hamiltonian, it is found that, through the variation of two structural parameters, the oscillatory system can be mono-stable, bi-stable and tri-stable, herein exhibiting three typical configurations of the structure. When the values of the other structural parameters are fixed, the reduction of the vertical distance between each rigid support and the horizontal beam may induce mono-, double- and triple-potential wells, successively. Because the vertical distance leading to triple-potential wells is too short to arrange, the cases of single-potential wells and double-potential wells are concentrated on.

When the ambient excitation in the original system is zero, considering the effect of the damping, the centers of the unperturbed system are all stable equilibria, which implies the stable equilibrium positions of the oscillator. Also, the initial positions can be these positions or be within a small vicinity of these positions. Therefore, in this study, the basins of attraction of the coexisted attractors that we really care about are those in the vicinity of these initial equilibrium positions. Even if an attractor's basin of attraction occupies the vicinity of an equilibrium and its fractal basin boundary is far beyond this vicinity, we believe that the basin of attraction is usable for practical applications. It is different from the works concerning the erosion of basins of attraction in the bistable beam systems [34–38].

In the case of mono-potential wells, the approximate forms and stabilities of the periodic solutions around the trivial center are analyzed via the method of multiple scales. Hard-spring characteristics are found in the oscillatory system; hence, the jump from a smaller-amplitude resonant response up to a larger-amplitude response can stem from the saddle-node bifurcation of resonant solutions. These can be triggered by the decrease in the frequency of the external excitation or the rise of the excitation level in a certain range, which is favorable for its applications such as kinetic energy collection and vibrating isolation. In the neighborhood of the critical values of the excitation for SN bifurcations, hidden attractors occur frequently.

In the cases of double-potential wells, the global dynamics of the oscillator is more complex. Intra-well and inter-well resonant responses are both investigated. For the analysis of the former, we also applied MMS. Similar to the case of the mono-potential well, the bistability within each potential well is easily observed. Differently, the system soft-spring characteristics; thus, the rise of the excitation frequency or level can lead to snapping through from the smallest periodic response to the other intra-well response with a higher amplitude. To analyze the inter-well resonant response, we utilized the average method. The theoretical prediction shows that, under a suitable excitation frequency, the rise of the excitation level may also lead to the presence of the inter-well resonant attractor, as validated by the numerical results. Based upon the evolutions of the coexisting attractors' basins of attraction with the rise of excitation level, snapping through among the four attractors within the potential wells and the one large-displacement attractor beyond the wells can be found and is due to a small perturbation of the initial state. Their seriously fractal basins of attraction show their high initial-condition sensitivity, even though they are not complex dynamical behaviors but are normal resonant responses. When the excitation level continues to increase, complex dynamical behaviors such as period-two attractors and chaos can be observed to coexist with the inter-well resonant behavior. The seriously fractal BA of chaotic response shows that chaos, the inherent initial-condition sensitive dynamical behavior, is also of initial-condition discontinuity, namely, another type of initial-condition

sensitivity. In contrast, as the period-two responses vanish and only two responses are left, i.e., an inter-well periodic response and chaos, the BA of chaos will become continuous with a smooth boundary. It implies that now chaos becomes locally stable and reliable, which is advantageous for the engineering applications of the structure because chaos represents a large displacement of its lumped mass.

The results in this work show that the adjustment of the vertical distance between the oscillator and the fixed pin can lead to different potential-well characteristics and the change of the usable frequency band for engineering applications such as vibration isolation and energy harvesting, which may provide theoretical references in utilizing multi-stability, the jump in the optimum structural design and the exploitation of geometrically nonlinear oscillating systems. Future research directions include the implementation of the structure and the investigation of the effects of structural parameters on the resonant responses via experimental efforts.

Author Contributions: Conceptualization, H.S.; methodology, H.S.; software, R.L.; validation, H.S. and R.L.; formal analysis, H.S.; investigation, R.L.; writing—original draft preparation, R.L. and H.S.; writing—review and editing, H.S.; visualization, R.L.; supervision, H.S.; project administration, H.S.; funding acquisition, H.S. All authors have read and agreed to the published version of the manuscript.

Funding: This research was funded by the National Natural Science Foundation of China, grant number 11472176.

Data Availability Statement: Data are contained within the article.

Conflicts of Interest: The authors declare no conflict of interest.

References

- Zhang, Y.; Cao, Q. The recent advances for an archetypal smooth and discontinuous oscillator. *Int. J. Mech. Sci.* **2022**, *214*, 106904. [[CrossRef](#)]
- Cao, Q.; Wiercigroch, M.; Pavlovskaja, E.E.; Grebogi, C.; Thompson, J.M.T. Archetypal oscillator for smooth and discontinuous dynamics. *Phys. Rev. E* **2006**, *74*, 046218. [[CrossRef](#)]
- Jiang, W.; Chen, L. Snap-through piezoelectric energy harvesting. *J. Sound Vib.* **2014**, *333*, 4314–4325. [[CrossRef](#)]
- Yang, T.; Cao, Q. Dynamics and high-efficiency of a novel multi-stable energy harvesting system. *Chaos Solitons Fractals* **2020**, *131*, 109516. [[CrossRef](#)]
- Ramlan, R.; Brennan, M.J.; Mace, B.R.; Kovacic, I. Potential benefits of a non-linear stiffness in an energy harvesting device. *Nonlinear Dyn.* **2009**, *59*, 545–558. [[CrossRef](#)]
- Han, N.; Cao, Q. A parametrically excited pendulum with irrational nonlinearity. *Int. J. Non-Linear Mech.* **2017**, *88*, 122–134. [[CrossRef](#)]
- Wu, B.; Liu, W.; Zhong, H.; Lim, C.W. A Modified Newton–Harmonic Balance Approach to Strongly Odd Nonlinear Oscillators. *J. Vib. Eng. Technol.* **2019**, *8*, 721–736. [[CrossRef](#)]
- Han, Y.; Cao, Q.; Ji, J. Nonlinear Dynamics of a Smooth and Discontinuous Oscillator with Multiple Stability. *Int. J. Bifurc. Chaos* **2016**, *25*, 1530038. [[CrossRef](#)]
- Adile, A.D.; Kenmogne, F.; Tewa, A.K.S.; Simo, H.; Tahir, A.M.; Kumar, S. Dynamics of a mechanical network consisting of discontinuous coupled system oscillators with strong irrational nonlinearities: Resonant states and bursting waves. *Int. J. Non-Linear Mech.* **2021**, *137*, 103812. [[CrossRef](#)]
- Kenmogne, F.; Noah, P.M.A.; Tafo, J.B.G.; Adoum, D.A.; Sali, M.; Abakar, M.T.; Eno, R.; Bell, E.Y. Stability of modulated signals in the damped mechanical network of discontinuous coupled system oscillators with irrational nonlinearities. *Arch. Appl. Mech.* **2022**, *92*, 3077–3091. [[CrossRef](#)]
- Han, N.; Cao, Q. Global bifurcations of a rotating pendulum with irrational nonlinearity. *Commun. Nonlinear Sci. Numer. Simul.* **2016**, *36*, 431–445. [[CrossRef](#)]
- Han, N.; Cao, Q. Rotating pendulum with smooth and discontinuous dynamics. *Int. J. Mech. Sci.* **2017**, *127*, 91–102. [[CrossRef](#)]
- Liu, C.; Jing, X.; Jiang, W.; Ding, H.; Chen, L.; Bi, Q. Bursting oscillation of a pendulum with irrational nonlinearity. *Int. J. Non-Linear Mech.* **2023**, *148*, 104299. [[CrossRef](#)]
- Yang, M.; Zhang, J.; Luo, X. Research on New Types of Suspension Vibration Reduction Systems (SVRSs) with Geometric Nonlinear Damping. *Math. Probl. Eng.* **2021**, *2021*, 6627693. [[CrossRef](#)]
- Li, Z.; Cao, Q.; Wiercigroch, M.; Leger, A. Analysis of the periodic solutions of a smooth and discontinuous oscillator. *Acta Mech. Sin.* **2013**, *29*, 575–582. [[CrossRef](#)]
- Chen, E.; Chu, B.; Wang, Y. Modelling and experimental investigations on the geometrical nonlinear dynamics of the SD oscillator. *Int. J. Model. Identif. Control.* **2016**, *25*, 190–198. [[CrossRef](#)]

17. Wang, J.; Huang, W.; Huang, L. Global dynamics and bifurcation for a discontinuous oscillator with irrational nonlinearity. *Commun. Nonlinear Sci. Numer. Simul.* **2023**, *119*, 107073. [[CrossRef](#)]
18. Han, Q.; Xu, W.; Sun, J. Stochastic response and bifurcation of periodically driven nonlinear oscillators by the generalized cell mapping method. *Phys. A Stat. Mech. Its Appl.* **2016**, *458*, 115–125. [[CrossRef](#)]
19. Han, Y.; Cao, Q.; Chen, Y.; Marian, W. A novel smooth and discontinuous oscillator with strong irrational nonlinearities. *Science China Physics. Mech. Astron.* **2012**, *55*, 1832–1843. [[CrossRef](#)]
20. Lai, S.K.; Wu, B.S.; Lee, Y.Y. Free vibration analysis of a structural system with a pair of irrational nonlinearities. *Appl. Math. Model.* **2017**, *45*, 997–1007. [[CrossRef](#)]
21. Zhang, X.; Yang, J. Power capture performance of an oscillating-body WEC with nonlinear snap through PTO systems in irregular waves. *Appl. Ocean. Res.* **2015**, *52*, 261–273. [[CrossRef](#)]
22. Qin, B.; Shang, H. Initial-Sensitive Dynamical Behaviors of a Class of Geometrically Nonlinear Oscillators. *Shock Vib.* **2022**, *2022*, 6472678. [[CrossRef](#)]
23. Han, N.; Liu, M. Dynamic Behavior Analysis of a Rotating Smooth and Discontinuous Oscillator with Irrational Nonlinearity. *Mod. Appl. Sci.* **2018**, *12*. [[CrossRef](#)]
24. Fakhreddine, H.; Adri, A.; Chajdi, M.; Rifal, S.; Benamar, R. A multimode approach to geometrically non-linear forced vibration of beams carrying point masses. *Diagnostyka* **2020**, *21*, 23–33. [[CrossRef](#)]
25. Yan, Y.; Zhang, Q.; Han, J.; Wang, W.; Wang, T.; Cao, X.; Hao, S. Design and investigation of a quad-stable piezoelectric vibration energy harvester by using geometric nonlinearity of springs. *J. Sound Vib.* **2023**, *547*, 117484. [[CrossRef](#)]
26. Ahmadi, A.; Parthasarathy, S.; Natiq, H.; Jafari, S.; Franovic, I.; Rajagopal, K. A non-autonomous mega-extreme multistable chaotic system. *Chaos Solitons Fractals* **2023**, *174*, 113765. [[CrossRef](#)]
27. Li, C.; Chen, G.; Kurths, J.; Lei, T.; Liu, Z. Dynamic transport: From bifurcation to multistability. *Commun. Nonlinear Sci. Numer. Simul.* **2021**, *95*, 105600. [[CrossRef](#)]
28. Castro, D.C.H.L.; Orlando, D.; Gonçalves, P.B. Static and dynamic nonlinear behavior of a multistable structural system consisting of two coupled von Mises trusses. *Int. J. Non-Linear Mech.* **2023**, *156*, 104510. [[CrossRef](#)]
29. Wang, Z.; Shang, H. Multistability and Jump in the Harmonically Excited SD Oscillator. *Fractal Fract.* **2023**, *7*, 7040314. [[CrossRef](#)]
30. Duc, H.D.; Ashraf, M.Z.; Do, V.T. Finite element modeling of free vibration of cracked nanoplates with flexoelectric effects. *Eur. Phys. J. Plus* **2022**, *137*, 447.
31. Pham, T.D.; Do, V.T.; Doan, T.L. Free vibration of Functionally graded sandwich plates with stiffeners based on the third-order shear deformation theory. *Vietnam J. Mech.* **2016**, *2*, 103122.
32. Nguyen, C.T.; Nguyen, T.T.; Do, V.T. New Numerical Results from Simulations of Beams and Space Frame Systems with a Tuned Mass Damper. *Materials* **2019**, *12*, 1329.
33. Dao, M.T.; Do, V.T.; Phung, V.M.; Nguyen, C.T.; Tran, N.D.; Dao, N.M. The application of the nonlocal theory and various shear strain theories for bending and free vibration analysis of organic nanoplates. *Mech. Based Des. Struct. Mach.* **2023**, *2023*, 2186893.
34. Harne, R.L.; Wang, K.W. A review of the recent research on vibration energy harvesting via bistable systems. *Smart Mater. Struct.* **2013**, *22*, 023001. [[CrossRef](#)]
35. Yang, K.; Harne, R.L.; Wang, K.W.; Huang, H. Investigation of a bistable dual-stage vibration isolator under harmonic excitation. *Smart Mater. Struct.* **2014**, *23*, 045033. [[CrossRef](#)]
36. Ilyas, S.; Younis, M.I. Resonator-based M/NEMS logic devices: Review of recent advances. *Sens. Actuators A* **2020**, *302*, 111821. [[CrossRef](#)]
37. Vagner, D.S.; Fernando, S.B.; Kelly, C.L.; Lbere, L.C.; Szezech, J.D.; Ricardo, L.V.; Murilo, S.B.; Antonio, M.B. Basin of attraction for chimera states in a network of Rossler oscillators. *Chaos* **2020**, *30*, 083115.
38. Bayani, A.; Rajagopal, K.; Khalaf, A.J.M.; Jafari, S.; Leutcho, G.D.; Kengne, J. Dynamical analysis of a new multistable chaotic system with hidden attractor: Antimonotonicity, coexisting multiple attractors, and offset boosting. *Phys. Lett. A* **2019**, *383*, 1450–1456. [[CrossRef](#)]

Disclaimer/Publisher's Note: The statements, opinions and data contained in all publications are solely those of the individual author(s) and contributor(s) and not of MDPI and/or the editor(s). MDPI and/or the editor(s) disclaim responsibility for any injury to people or property resulting from any ideas, methods, instructions or products referred to in the content.